Optical Fiber Technology 88 (2024) 103947

Contents lists available at ScienceDirect

Optical Fiber Technology

journal homepage: www.elsevier.com/locate/yofte

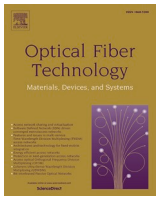

Regular Articles

Highly sensitive magnetic field sensor based on magnetic sensitive adhesive cavity

Mengjie Wang [a], Xin Ding [b,c], Rongfu Zhang [a,*]

[a] University of Shanghai for Science and Technology, School of Optical-Electrical and Computer Engineering, No. 516 Jungong Road, Yangpu District, Shanghai, 200093, China
[b] Shenzhen University, College of Physics and Optoelectronic Engineering, Shenzhen, 518060, China
[c] Guangdong Laboratory of Artificial Intelligence and Digital Economy, Shenzhen, 518060, China

ARTICLE INFO

Keywords:
Fabry-Perot cavity
Fiber optic sensor
Ferrofluid
Magnetic field measurement

ABSTRACT

A Fabry-Perot (FP) fiber optic sensor utilizing ferrofluid nanomaterials is proposed for magnetic field measurements. A magnetic sensitive adhesive (MSA) is synthesized through the homogeneous blending of ferrofluid and UV glue, serving as a magnetic field-sensing material and adheres to the neatly cut single-mode fiber (SMF) surface to form a FP interferometer. With the increase of the magnetic field, the MSA cavity is subjected to the magnetic force, which causes the elongation of the MSA cavity and induces to the wavelength drift of the reflection spectrum. Experimental results show that the magnetic field sensor exhibits a sensitivity of up to 6.12 nm/mT within the range of 1 to 4 mT, with high linearity and low temperature crosstalk. The sensor's compact structure, facile manufacturing, and adaptability render it suitable for detecting slit leakage magnetic fields and high-precision magnetic fields.

1. Introduction

Magnetic fields, as a crucial metric in physical parameters, find widespread application in various domains such as aerospace, medical, electric power industry, and architecture [1,2]. Due to the prevalence of optical fibers, magnetic field sensors (MFSs) based on various interference principles have garnered researchers' attention. In comparison to electronic MFSs, optical fiber sensors offer advantages such as compactness, stability, robustness, and corrosion resistance. Types of magnetic field optical fiber sensors include Surface Plasmon Resonance (SPR) [3–5], Mach-Zehnder Interferometer (MZI) [6–8], fiber gratings [9–11], and Fabry-Perot Interferometer (FPI) [12–14]. SPR structures typically necessitate the excitation of plasmon resonances on metal films, requiring precise control over the thickness of the metal film. MZI structures involve processes like tapering [15,16], bending [17,18], and offset fusion splicing [19,20], significantly compromising the mechanical strength of the structure. Fiber gratings require laser inscription, making the structure fragile and prone to breakage. The FPI structure, with its compactness and straightforward fabrication, is suitable for scenarios involving narrow gaps or magnetic field leakage.

Optical fibers, composed of materials such as silica or plastic, exhibit immunity to the influence of magnetic fields. Their responsiveness to magnetic fields comes from the synergistic combination of functional materials and various structures. Magnetic-sensitive materials applied to optical fibers can be categorized into three types: magnetostrictive materials, magneto-refractive materials, and magneto-rheological materials. Magnetostrictive materials undergo alterations in length under the influence of a magnetic field. Combining this effect with the optical fiber's sensitive structure effectively reflects the magnetic field. In 2021, Peng et al. [11] combined the Terfenol-D as magnetostrictive material with a Fiber Bragg Grating, achieving a structure sensitivity of 9.83 pm/mT. Despite directed manipulation of magnetic domains, the limited length variation due to the magnetostrictive effect resulted in a minor change in the grating period, leading to lower sensitivity. In 2023, Xu et al. [21] integrated a Terfenol-D bar with the FPI. The Fabry-Perot cavity responds sensitively to changes in cavity length, yielding a sensitivity of 811.53 pm/mT. However, its dimensions are approximately 3 cm constrained by the length of the Terfenol-D bar. Magnetic field sensors employing magnetostrictive materials are constrained by the inherent properties of these materials, often resulting in larger dimensions and lower sensitivity. Consequently, there has been widespread application of magneto-refractive materials in diverse structures to fabricate fiber-optic sensors in recent years.

Magnetic fluid (MF), primarily employed as a magneto-refractive

* Corresponding author.
E-mail address: zrf@usst.edu.cn (R. Zhang).

https://doi.org/10.1016/j.yofte.2024.103947
Received 4 June 2024; Received in revised form 6 August 2024; Accepted 18 August 2024
Available online 9 September 2024

material, consists of ferromagnetic nanoparticles, surfactants, and dispersants [22,23]. The disordered magnetic nanoparticles in the MF form uniformly distributed magnetic chains under the magnetic field, causing a change in the refractive index of the MF. In 2023, Ding et al. [8] combined ferrofluid with a balloon-like interferometer, which is sensitive to changes in refractive index [24,25]. Utilizing the magneto-refractive effect, a sensitivity of 0.683 nm/mT is achieved in the range of 0 to 10 mT. The device is simple to fabricate and has dimensions of approximately 8 mm. Zhao et al. [26] integrated ferrofluid with the FPI, exploiting the MF's magneto-volume effect to attain a sensitivity of −4219.15 pm/Gs, with a sensing head length of 50 μm. Duan et al. [27] filled the FP air cavities with MF and polydimethylsiloxane (PDMS) for temperature and magnetic field detection, whose magnetic field intensity sensitivity raised to −2245 pm/mT. For this structure, due to the small volume of the MF, precise filling and stable encapsulation processes are required to avoid the risk of leakage. In contrast to MFs, magnetic rheological elastomers, initially a viscous liquid during fabrication, solidify after encapsulation, significantly enhancing structural stability and mechanical strength. Comprising ferromagnetic particles and a soft base material, magnetic rheological elastomers undergo volume changes under the influence of a magnetic field and revert to their original state after the field is removed.

In this work, a magnetic sensitive adhesive (MSA) with UV glue as the base material and MF as the dopant for magnetic field sensing, combined with SMF to fabricate a FPI magnetic field sensor. Due to the molecular tension on the surface of the droplet, the liquid-like MSA forms a smooth MSA cavity on the end face of the SMF. For the quality of FPI reflection spectrum, FPI with different doping concentrations and different lengths were made and their reflection spectra were measured and compared. The experimental results show that the sensitivity of the sensor is −6.12 nm/mT in the range of 1mT to 4mT. In addition, the sensor has good stability, and has low temperature cross sensitivity, which makes it an attractive solution in the field of high sensitivity magnetic field measurement.

2. Fabrication of FPI and measurement principle

A schematic diagram of the fabrication of the FPI sensor was illustrated in Fig. 1. The MSA was made by mixing MF and UV glue in a certain ratio as is shown in Fig. 1(a). This mixture was stirred and then sonicated in an ice-water mixture for 1 h. Subsequently, a cut fiber (SMF1) was immersed in the MSA, resulting in the formation of spherical MSA droplets on the end face of SMF1 due to liquid molecular tension, as shown in Fig. 1 (d). The SMF1 with MSA end face was moved by fusion splicer to touched another cleaved fiber (SMF2), which makes the FPI (Fig. 1(e)(f)). The FPI was cured by exposure to a UV lamp for 30 min in Fig. 1(g). To safeguard the fabricated sensing head from environmental erosion, a capillary tube was affixed to the outside of SMF2 and secured with UV glue for encapsulation of the sensing head. The microscopic picture after encapsulation was presented in Fig. 1(h). FPIs with different MSA cavity lengths are fabricated by controlling the end face contact time in Fig. 1(e).

The sensing system comprises an ultra-wideband light source (UWLS, Golight), a spectrum analyzer (OSA, Yokogawa, AQ6370D), a circulator, and the FPI structure. The light emitted by the UWS enters the FPI through the circulator, and the output spectrum is collected and displayed by the OSA. Due to the presence of the MSA cavity, the light entering the FPI passes through two reflecting mirrors, namely M1 and M2, exciting two beams of reflected light, as shown in the inset of Fig. 2. The interference spectrum of the Fabry-Perot cavity is formed by the interference of the two reflected lights, which is expressed as [17]

$$I = I_1 + I_2 + 2\sqrt{I_1 I_2}\cos(4\pi n_M L_M/\lambda_1) \\ I_1 = R_1, I_2 = (1-R_1)^2(1-r_M)^2 R_2 \quad (1)$$

Where I_1 and I_2 are the reflection intensity of M1 and M2, r_M is the transmission loss of MSA cavity. n_M is the effective refractive index of the

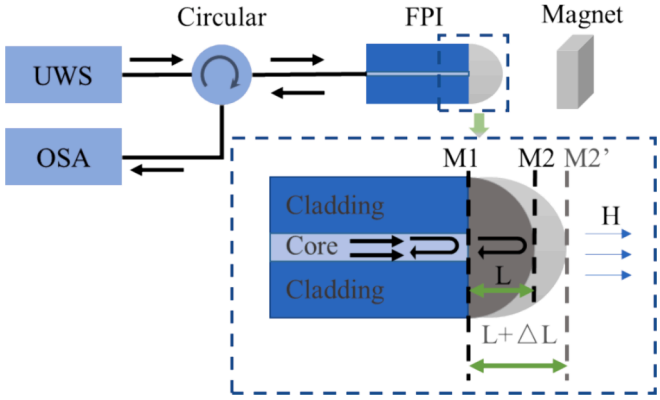

Fig. 2. Schematic diagram of the fiber sensor system.

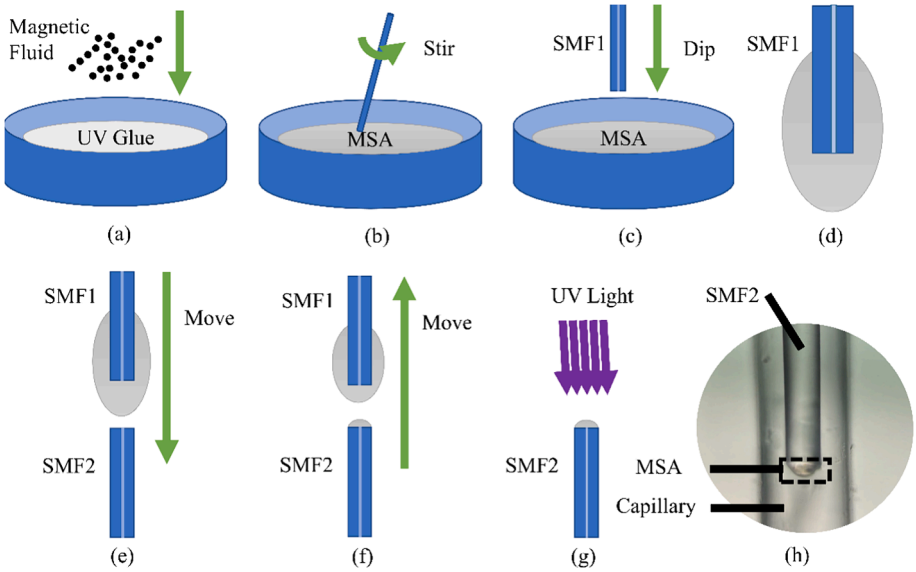

Fig. 1. Fabrication of the fiber sensor.

MSA, L_M is the length of the MSA cavity, and R_1, R_2 are the reflectivity of M1 and M2, respectively, which is calculated by $R_1 = [(n_{SMF} - n_M)/(n_{SMF} + n_M)]^2$, $R_2 = [(n_M - n_{air})/(n_M + n_{air})]^2$. The resonant dip is satisfied

$$4\pi n_M L_M/\lambda_m = (2m+1)\pi, m = 0, 1, 2... \quad (2)$$

Where m is the order. As the external inductive magnetic field increases to B_0, the MSA tip is subjected to the magnetic field force leading the elongation of MSA, which is described by [28]

$$\Delta L_M = -\frac{7-4\nu}{4G(7+5\nu)}\left[(\mu_r-1)^2+\frac{\Delta b}{\mu_0}\right]\frac{3B_0^2}{\mu_0(\mu_r+2)^2} \quad (3)$$

Where ν is the Poisson ratio, and $G{=}G_0\,(1+2.5\varphi+14.1\varphi^2)$ is the shear modulus. Here G_0 is the shear modulus of the pure polymer and φ is the volume fraction of magnetic particles. μ_0 and μ_r are the magnetic permeability of vacuum and the relative magnetic permeability of the MSA material. Coefficients Δb represents the normal components of strain. As a result, the mirror M2 moves to M2′, causing the drift of the resonant dip, as is expressed in Eq. (4).

$$\Delta\lambda_m = 4\pi n_M \Delta L_M/(2m+1) \quad (4)$$

In Eq. (4), the relationship between the length change and the shift in resonant dip is evidently linear. Consequently, the magnetic field can be determined by monitoring the variation in the resonance dip in the reflection spectra as follows

$$\Delta\lambda_m = K\Delta B \quad (5)$$

Here, K is the sensitivity of magnetic field. ΔB is the variation of the external inductive magnetic field. The drift of the resonant dip is related to the free spectral range (FSR), which is the distance between two resonant dips and is defined by $FSR = \lambda_{m+1} - \lambda_m = \lambda_{m+1}\lambda_m/2n_M L_M$. Notably, the FSR depends on the length of the MSA cavity. The observable change in MSA cavity length is more pronounced with increased magnetic field, a phenomenon influenced by the proportion of doped magnetic particles in the substrate, thereby defining the mass fraction of MF within the MSA

$$\alpha = \frac{\omega_{\mathrm{MF}}}{\omega_{mix}} \times 100\% \quad (6)$$

Here, $\omega_{\mathrm{MF}}, \omega_{mix}$ represent the mass of MF and mixture, respectively. For MSA, a higher ratio of magnetic particles enhances the magnetic response. However, an excessive amount of magnetic particles lead to an uneven end face of the FPI [29], impacting the quality of the reflection spectrum.

3. Experimental results and discussion

3.1. The length and concentration of MSA

In pursuit of an optimal reflection spectrum, we tested a series of FPIs with MSA to ascertain the most effective configuration. The MSA was made by mixing UV glue (Ergo 8500, Kisling) and water-based MF (EMG605, Ferrotec Inc.). The refractive index of UV glue is 1.4826, measured by Abbe refractometer (WAY-2WAJ, Lichen). The elastic modulus and Poisson's ratio of materials were measured using electronic universal testing machine (MTS E44.304) using middle parallel section size of 12 mm × 2 mm × 1 mm. The Elastic modulus and Poisson's ratio are 6.74 MPa and 0.145. The magnetic particle concentration and density of water-based MF are 3.9 % and 1.18×10^3 kg/m^3, respectively. As is shown in Eq. (3), the elongation of MSA is dependent on the volume fraction φ. Hence, the relationship between elongation of MSA and φ is displayed in Fig. 3. The parameters are $\mu_0 = 1$, $\mu_r = 1.18$, and $\Delta b = 1 \times 10^{-4}$. In Fig. 3, the elongation of MSA has an opposite trend with increase

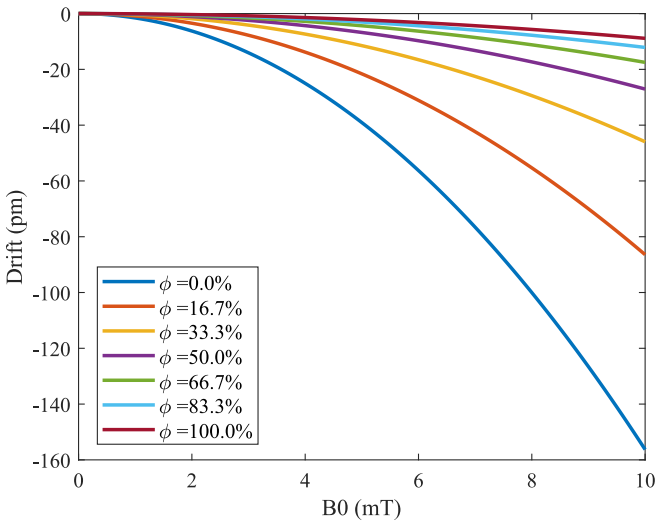

Fig. 3. The elongation of MSA with increasing inductive magnetic field in different φ.

of φ at same inductive magnetic field. The fastest decreasing curve is the volume fraction $\varphi = 0$ %. However, the relative magnetic permeability disappears in this case. Hence, the α value of MSA is fabricated as small as possible.

Various FPIs were prepared, each characterized by different mass fractions and lengths of the MSA. Specifically, the α values for these FPIs were 49.9 %, 40.1 %, 29.7 %, 16.7 %, 9.1 %, and 1.6 %, and the corresponding lengths of MSA were 11.5 μm, 21.5 μm, and 43 μm. The resultant reflection spectra are depicted in Fig. 4.

In Fig. 4, all the FPIs show spectral periodicity. As depicted in Fig. 4 (a), for MSA with mass fraction (α) of 49.9 %, the amplitude of reflection intensity of FPIs with cavity lengths of 11.5 μm, 21.5 μm and 43 μm is about 5 dB. According to Fig. 4(b), the reflection spectra of different lengths manifest insufficient smoothness, with a noticeable jitter phenomenon occurring in the resonant dip, impeding the identification of the resonant dip. Conversely, the reflection intensity of FPIs with three lengths are uniform, and the position of resonant dip is relatively obvious in Fig. 4(c)(d). In Fig. 4(e), for MSA with α = 9.1 %, the reflection amplitude of FPI with cavity length 43 μm is less than 4 dB, and the amplitude difference between FPI with cavity length 11.5 μm and 21.5 μm is large. For $\alpha = 1.6$ % (Fig. 4(f)), the intensity amplitude is less than 4 dB, which is close to the reflection spectrum of UV glue. As a result, mass fraction α = 29.7 % and 16.7 % were chosen for further experiments. The number and parameters of the fabricated FPIs are shown in Table 1.

3.2. Optimization of measured spectra

To minimize the location error of the resonant dip, we perform Fast Fourier Transform (FFT) analysis on the reflection spectra in Fig. 5. Taking Sample B1 in Fig. 4 (d) as an example, the FFT analysis of the spectra before and after FFT filtering is shown in Fig. 5(a). There is a main peak appearing around 0.01 nm^{-1} in the figure. The reflection spectrum around the bandwidth of the main peak is extracted and used as a measurement based on the FFT analysis. After the filtering process, the FFT analysis of the filtered spectrum reveals only a predominant peak at 0.01 nm^{-1}, and the corresponding spectrum, as indicated by the red line in Fig. 5(b), is noticeably smoother. And the FSR of original and filtered spectra are both 100 nm, which is consistent with FFT peak 0.01 nm^{-1}.

Furthermore, the filtered spectra affect the measurement results as is shown in Fig. 6. The sensitivity of the original reflection spectra is −1.636 nm/mT and the linearity is 0.9068 in the range of 1mT to 9 mT.

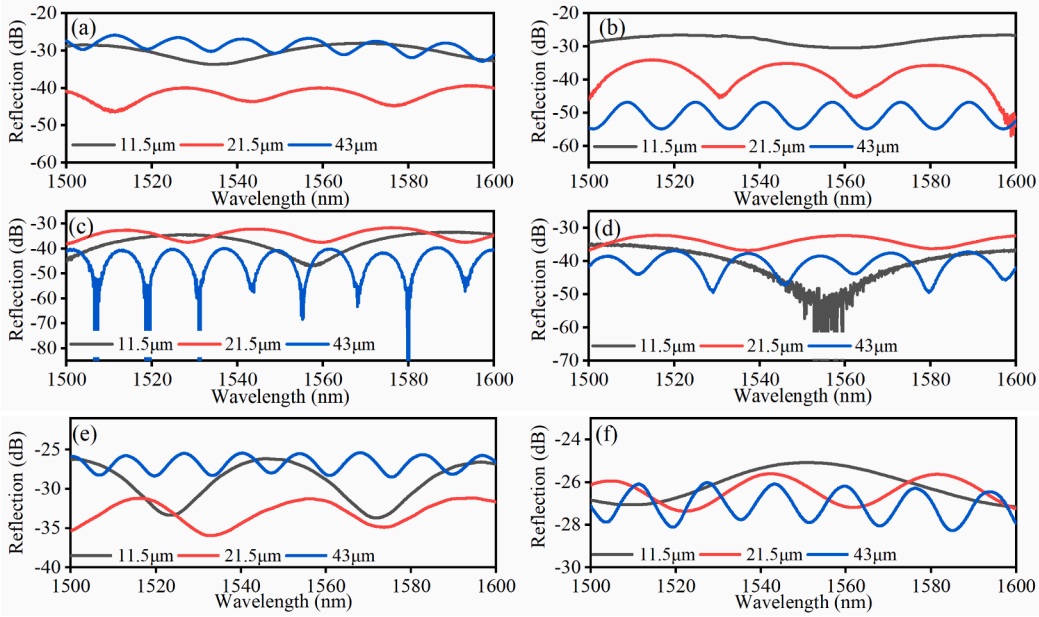

Fig. 4. Reflection spectra of FPI in (a) α = 49.9 %, (b) α = 40.1 %, (c) α = 29.7 %, (d) α = 16.7 %, (e) α = 9.1 %, (f) α = 1.6 %.

Table 1
Number and parameters of the fabricated FPIs.

Number	L_M (μm)	α (%)
A1	11.5	29.7
A2	21.5	
A3	43	
B1	11.5	16.7
B2	21.5	
B3	43	

However, after FFT filtering, the sensitivity is −1.56 nm/mT, and the linearity is 0.94289. The sensitivity after FFT filtering is lower than the sensitivity without filtering, but the linearity is increased. Therefore, FFT filtering of the collected spectrum can restore the linearity of the sensor and remove the noise in the spectral signal to a certain extent. As for the measured spectra have some slight burrs (Sample A1), the burrs affect the tracking of resonant dip, which is shown clearly in Fig. 7 (c). FFT filters out some useless noise, makes the spectral data smoother, and facilitates tracking the position of dip.

3.3. Magnetic field measurement

For the magnetic field experiment, the structure was positioned between the poles of two permanent magnets, resulting in an almost uniform magnetic field. The magnetic field is changed by adjusting the distance between the two permanent magnets, and is calibrated in real time using a Gaussian meter (HT20, Shanghai Hengtong). The detect range of the Gaussian meter is between 0 mT and 200 mT, whose resolution is 0.1mT. The saturation magnetization of thin films magnetic fluid is 10 mT [12]. A range of magnetic field from 1 mT to 9 mT was applied to the sensing probe, yielding nine sets of magnetic field measurements at intervals of 1mT. The shift of the resonant dip reflects the change of the magnetic field. To ensure measurement accuracy, the ambient temperature was kept at 20 °C, and the spectra were recorded after the magnetic field was stabilized for 5 min before each measurement.

For FPIs with MSA mass fraction α of 29.7 %, the reflection spectra shown in Fig. 8 are obtained after FFT filtering of the collected reflection spectra. Fig. 8 (a) to (c) all show that the MSA cavity length increases and the resonant dip shifts to short wavelength as the magnetic field strength increases, which is consistent with the aforementioned

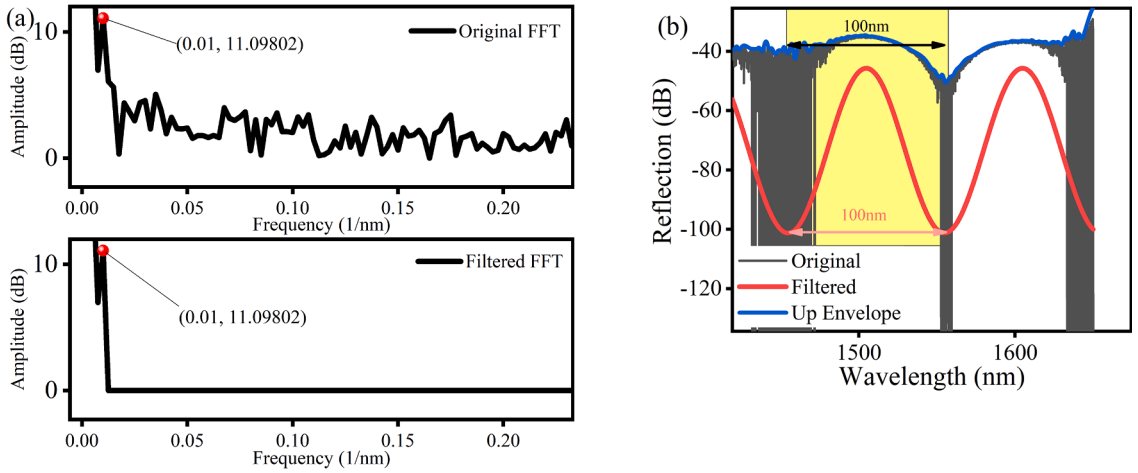

Fig. 5. (a) FFT analysis of original and filtered reflection spectra. (b) Corresponding reflection spectra.

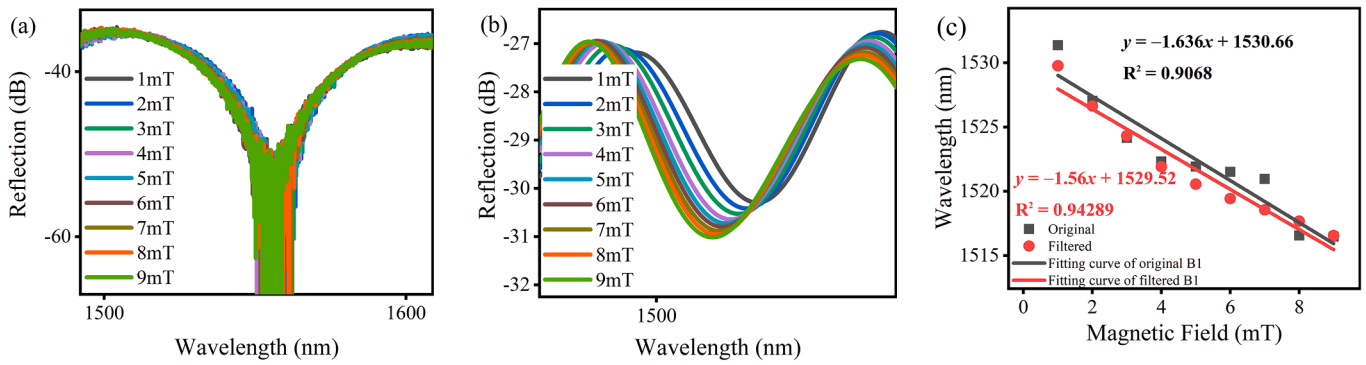

Fig. 6. (a) Original and (b) FFT filtered reflection spectra of B1. (c) Corresponding sensitivities.

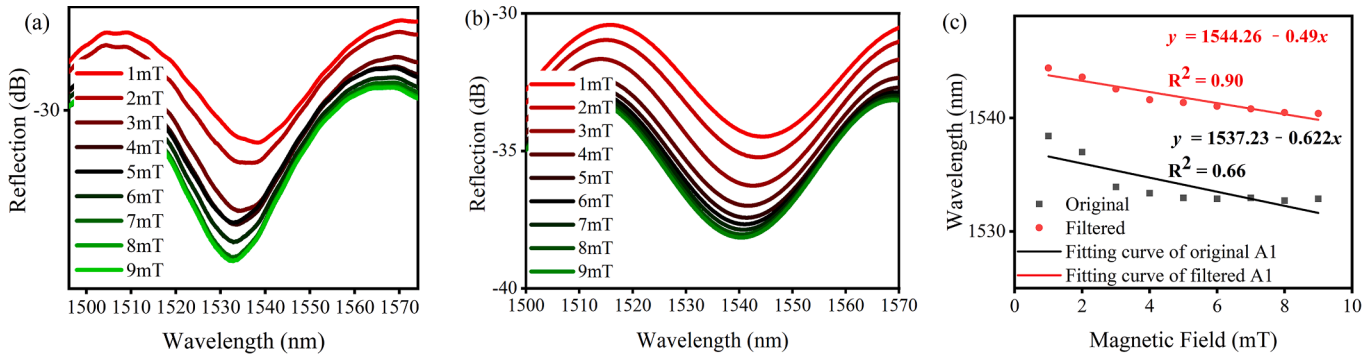

Fig. 7. (a) Original and (b) FFT filtered reflection spectra of A1. (c) Corresponding sensitivities.

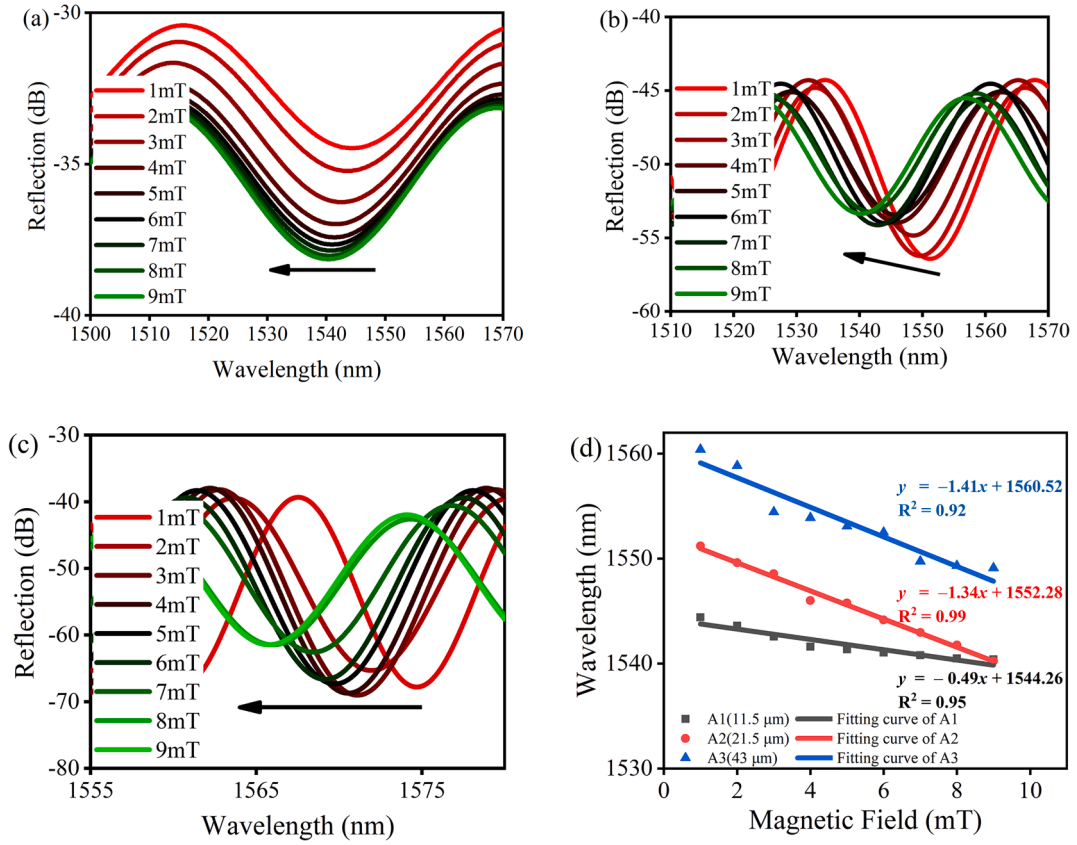

Fig. 8. Reflection spectra of (a) A1, (b) A2, and (c) A3; (d) relations between resonant dip and magnetic field for A1, A2, and A3.

analysis. The resonant dip of A1, A2, and A3 are linearly fitted to the magnetic field to obtain Fig. 8 (d).

In Fig. 8 (d), within the range of 1 mT to 9 mT, the sensitivities of A1, A2 and A3 are −0.49 nm/mT, −1.34 nm/mT, and −1.41 nm/mT, with corresponding linearities of 0.95, 0.99, and 0.92, respectively. As the cavity length increases from 11.5 μm to 43 μm, the number of doped magnetic particles in the MSA cavity length increases, the amount of wavelength shift greatly increases, and the ability of the sensor to sense the magnetic field increases.

For the MSA cavity with α = 16.7 %, the reflection spectra of the FPI of all three lengths are blue-shifted as the magnetic field increases. As the magnetic field increases from 1mT to 9mT, the resonant dips of B1, B2 and B3 shift from 1529.76 nm, 1579.68 nm and 1583.04 nm to 1516.56 nm, 1561.04 nm and 1551.44 nm, respectively. Through linear fitting analysis of the resonant dip shift against its corresponding magnetic field, the resulting relationship is illustrated in Fig. 9(d). Within the magnetic field range of 1 mT to 9 mT, the magnetic field sensitivity of B1 is −1.56 nm/mT. For B2 and B3, the drift of resonant dip decreases as the magnetic field increases. The magnetic field sensitivity of B2 is −2.67 nm/mT in 1 mT~7 mT. The FSR of B3 is 18.32 nm in wavelength range of 1550 nm and 1580 nm as is shown in Fig. 9(c). To accurately capture the spectral shifts and to account for the magnetic field's impact, the detection range is divided into two segments: 1mT to 4mT and 5mT to 9mT. The magnetic field sensitivities of B3 are −6.12 nm/mT in 1 mT~4 mT, and −2.53 nm/mT in 5 mT~9 mT, respectively. Additionally, the minimum resolution of OSA is 0.02 nm. Combined with its inherent value, the minimum resolution attainable by the sensor in quantifying magnetic field can be determined through the utilization of the following equation.

$$\Delta H = \frac{0.02\ \text{nm}}{6.12\ \text{nm/mT}} = 0.00033\ \text{mT} \tag{7}$$

3.4. Temperature cross-sensitivity of the proposed FPI

As both UV glue and MF are responsive to temperature, the proposed FPI structure may be affected by temperature variations. To assess this, we conducted measurements on the B3 using a thermostat within the temperature range of 29.2 °C to 49.2 °C. The resulting reflection spectrum of its temperature response is presented in Fig. 10(a), accompanied by the corresponding curve fitting in Fig. 10(b). According to Fig. 10(b), the temperature sensitivity of the B3 is determined to be 282.72 pm/℃. Considering the magnetic field sensitivity of the structure as 6.12 nm/mT and 2.53 nm/mT, the estimated temperature cross-sensitivity of the sensor are approximately 0.046 mT/°C (0.28/6.12 = 0.046) and 0.11 mT/°C (0.28/2.53 = 0.11). This suggests that temperature has minimal impact on the accuracy of the magnetic field measurements using this sensor.

3.5. Stability and repeatability

The stability of the FPIs is recorded for 30 min when the magnetic fields stabilized at 7 mT, and the results are shown in Fig. 11. In Fig. 11, δ represents the maximum wavelength drift, and σ denotes the standard deviation of the test. Fig. 11(a) and (b) display the short-term test results for samples A1 to A3 and B1 to B3, respectively. The test reveals that over a 30-minute period, the maximum resonant wavelength drift for A1 to A3 are 0.08 nm, 0.08 nm, and 0.04 nm, corresponding to magnetic field changes of 0.0392 mT, 0.1072 mT, and 0.0564 mT, respectively. For B1 to B3, the maximum resonant wavelength drift is consistently 0.12 nm, with corresponding magnetic field changes of 0.1872 mT, 0.3204 mT, and 0.7344 mT. The standard deviation for each sample's test results is calculated, with A1 to A3 having standard deviations of 0.0163 nm, 0.031 nm, and 0.031 nm, and B1 to B3 having standard

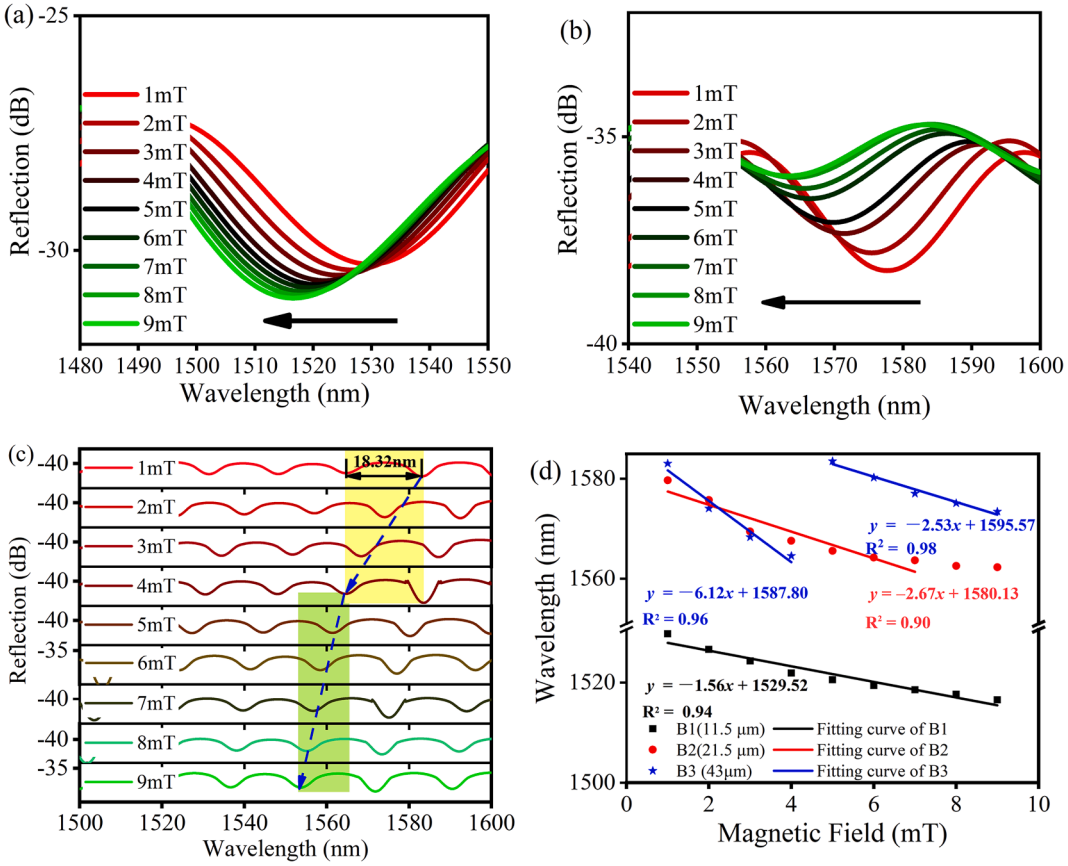

Fig. 9. Reflection spectra of (a) B1, (b) B2, (c) B3; (d) relations between resonant dip and magnetic field for B1, B2, and B3.

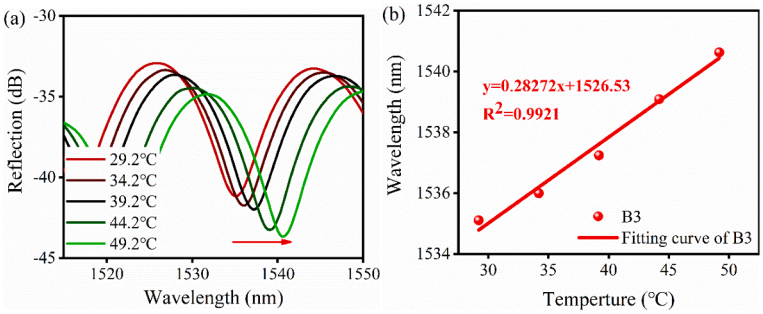

Fig. 10. (a)Reflection spectra of B3 in different temperatures. and (b) Linear fitting of dip.

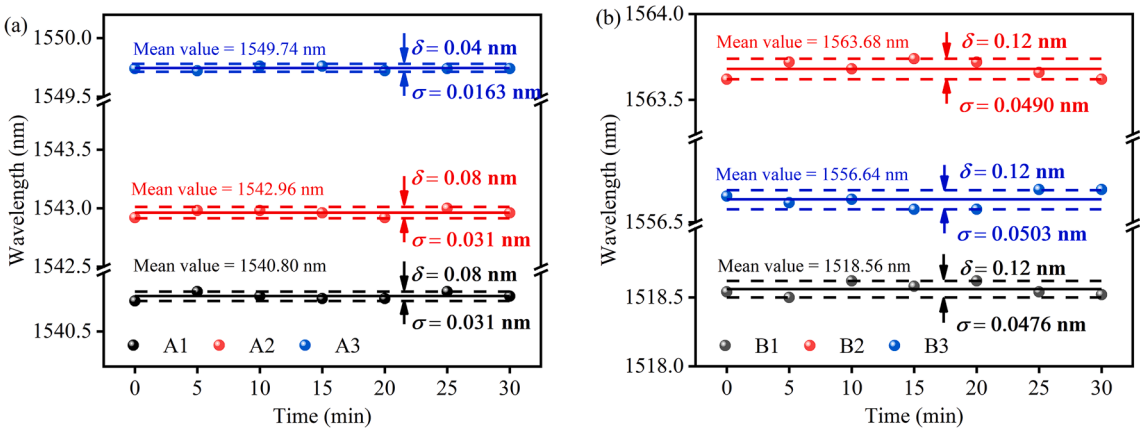

Fig. 11. Stability of the sensing system.

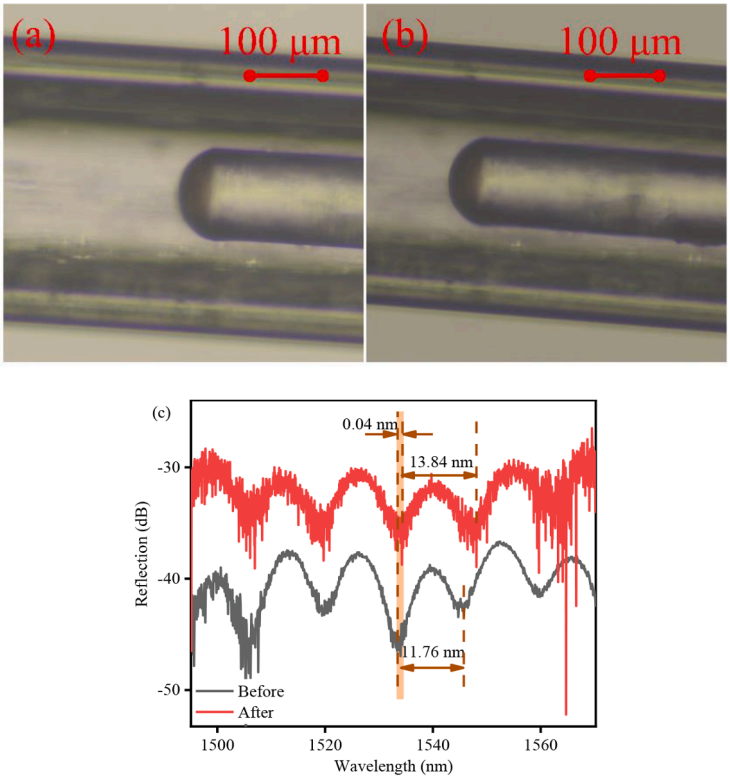

Fig. 12. The side views of B3 (a) before and (b) after a month, (c)the spectra of B3.

deviations of 0.0476 nm, 0.0490 nm, and 0.0503 nm, respectively.

Furthermore, considering the potential degradation risk of MSA materials, Fig. 12 illustrates the side views of the B3 structure in a month. The views indicate that the shape of the MSA structure remains unchanged. The corresponding spectra of the structure before and after one month are shown in Fig. 12 (c). After one month, the free spectral range of the spectrum changes from 11.76 nm to 13.84 nm, and the resonant wavelength position changes from 0.04 nm.

Fig. 13 illustrates the magnetic response of the proposed sensor during both increasing and decreasing magnetic field cycles. The maximum deviation of the magnetic sensitivity is ± 0.33 nm/mT, with an average magnetic sensitivity of 6.00 nm/mT. The repeatability error is quantified at ± 5.5 %.

3.6. Comparation with other sensors

The proposed sensor is compared with some recent studies in terms of sensitivity, range, size and fabrication complexity in Table 2. The sensitivity of the SPR sensor [3031] is reported at 1.10 nm/mT and 1.56 nm/mT, respectively, whereas the lengths are longer than that of the proposed sensing head. Additionally, the SPR sensor in [23] necessitates coating treatment and sealing of the MF, introducing the risk of leakage. Also, the SPR structure requires grinding of the optical fiber and metal coating, which makes the fabrication cost of the sensor greatly increased. The cladding-etched long-period grating [32] boasts a higher magnetic field sensitivity compared to the proposed FPI, but its operational range is more restricted due to its length. And the production process of LPG in [32] is complex, and the rate of defective products may be high. Balloon-like interferometers [8], while easy to fabricate, exhibit a lower magnetic field sensitivity than the proposed structure. The magnetic PDMS FPI [14] achieves a sensitivity of 563.2 pm/mT with a reduced size of 1 mm. Compared to PDMS, UV glue not only features a shorter curing time but also exhibits lower temperature sensitivity. It is noteworthy that Fe_3O_4 nanoparticles in MF possess favorable magnetic responsiveness, which are more suitable for fabricating magnetic sensitive materials.

The fiber tip cantilever structure [33] is intricate, involving two-photon beam printing and incurring high costs. The FPI sensor in [34] is both sensitive to magnetic field and compact, yet it carries the risk of MF leakage. The fiber Bragg grating with a Terfenol-D bar [10] achieves sensitivity at 9.83 pm/mT in range from 0 mT to 140 mT, demonstrating insensitivity to slight variation of magnetic field. However, this configuration may encounter limitations in restrictive detection environments, such as slits. The grating structure [35] has low mechanical strength, and the sensitivity is 0.2186 nm/mT, which is far lower than the proposed structure. Compared to [36], the proposed structure has a compact structure. The proposed sensor, with an excellent cost-performance ratio, excels in magnetic field detection with its efficient capabilities and cost control. Its features of easy manufacturability, low production cost, high sensitivity, compact size, and simple structure ensure its widespread application scenarios.

4. Conclusion

A FPI sensor utilizing a MSA is proposed, where the MSA composes a blend of MF and UV glue. The MSA can be completely cured after only half an hour of irradiation with UV lamp. The sensing head is fabricated by dip the neat SMF end face in MSA, which is simple to fabricate and low-cost. Since this MSA cavity contains magnetic particles, when the external magnetic field strength increases, this MSA cavity will elongate and cause the wavelength shift of the reflection spectrum of the FPI. The sensor has a magnetic field sensitivity of 6.12 nm/mT in the range of 1mT~4mT. Furthermore, the sensor exhibits excellent stability, with a temperature cross-sensitivity of only 0.046 mT/°C. The structure offers distinct advantages in detecting magnetic leakage and slits.

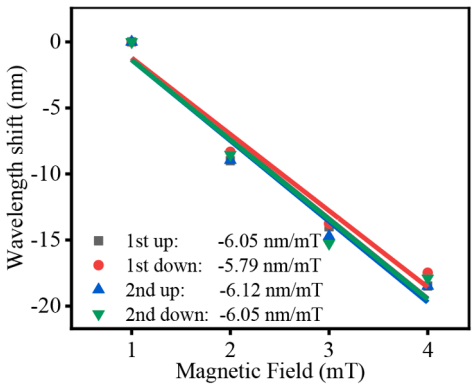

Fig. 13. Repeatability of the sensing system.

Table 2
Comparisons of optical fiber magnetic field sensors.

Measurement Configuration	Magnetic Field Sensitivity (nm/mT)	Range (mT)	Length (μm)	Fabrication Complexity
SPR with MF [30]	1.10	6.2 ~ 16.3	125	Complex
SPR with MF [31]	1.56	0 ~ 6.03	15,000	Complex
Balloon-like Interferometer [8]	0.683	0 ~ 10	14,000	Easy
Cladding-etched long period grating [32]	44.69	3 ~ 7.4	16,560	Complex
Magnetic PDMS FPI [14]	0.5632	0 ~ 4	100	Easy
Fiber-Tip Microcantilever [33]	0.119	0 ~ 90	50	Complex
Fiber Tip with MF [34]	1.54	1 ~ 8	100	Complex
Fiber Bragg Grating with Terfenol-D [10]	0.00983	0 ~ 140	45,000	Easy
Long Period Grating cascaded with FBG [35]	0.2186	1 ~ 8	500	Complex
Dual-Core Photonic Crystal Fiber with MF [36]	1.562	0–10	4000	Easy
This work	**6.12**	**1 ~ 4**	**43**	**Easy**

CRediT authorship contribution statement

Mengjie Wang: Writing – review & editing, Writing – original draft, Visualization, Validation, Software, Methodology, Investigation, Formal analysis, Data curation, Conceptualization. **Xin Ding:** Writing – review & editing, Writing – original draft, Methodology, Investigation. **Rongfu Zhang:** Writing – review & editing, Supervision, Resources, Project administration.

Declaration of competing interest

The authors declare that they have no known competing financial interests or personal relationships that could have appeared to influence the work reported in this paper.

Data availability

Data will be made available on request.

Acknowledgements

This work was supported by National Key Research and Development Program of China (2022YFF0706003).

References

[1] Cañada J, Kim H. and Velásquez-García L F. Three-dimensional, soft magnetic-cored solenoids via multi-material extrusion, Virtual and Physical Prototyping, 2024; 19(1) e2310046 :1-18.
[2] L. Vancini, M. Mengoni, G. Rizzoli, L. Zarri, A. Tani, Local Demagnetization Detection in Six-Phase Permanent Magnet Synchronous Machines, IEEE Transactions on Industrial Electronics 71 (6) (2024) 5508–5518.
[3] M.R. Islam, et al., Design of a quad channel SPR-based PCF sensor for analyte, strain, temperature, and magnetic field strength sensing, Opt. Quant. Electron. 54 (2022) 563.
[4] E. Ilbeygi, M. Jahanbakhshian, M.A. Pirlar, R. Karimzadeh, Magnetic field sensor based on plasmonic fiber optics coupled with smartphone, Opt. Laser Technol. (2021:) 140 107065.
[5] N. Cennamo, F. Arcadio, V. Marletta, S. Baglio, L. Zeni, B. Ando, A magnetic field sensor based on SPR-POF platforms and ferrofluids, IEEE Trans. Instrum. Meas. 70 (2021) 1–10.
[6] H.C.A.S.G. Vasconcelos, J.M.M.M. Almeida, C.M.T. Saraiva, Jorge P A d S, Coelho L C C, Mach-Zehnder interferometers based on long period fiber grating coated with titanium dioxide for refractive index sensing, J. Lightwave Technol. 37 (2019) 4584–4589.
[7] A. Layeghi, H. Latifi, Tunable ferrofluid magnetic fiber sensor based on nonadibatic tapered Hi-Bi fiber in fiber loop mirror, J. Lightwave Technol. 36 (2018) 1097–1104.
[8] X. Ding, N. Chen, T. Jin, X. Zhang, R. Zhang, Temperature-compensated balloon-like fiber magnetic field sensor with F-P structure based on PDMS, Opt. Laser Technol. 162 (109302) (2023) 1–9.
[9] Y. Zhu, C. Jiang, Y. Ma, Z. Liu, C. Mou, Y. Liu, Ultrasensitive magnetic field sensor based on cladding-etched long-period grating, Opt. Lett. 48 (2023) 2461–2464.
[10] C. Jiang, Y. Liu, C. Mou, J. Wen, S. Huang, T. Wang, Fiber Vector Magnetometer Based on Polarization-Maintaining Fiber Long-Period Grating with Ferrofluid Nanoparticles, J. Lightw. Technol. 40 (8) (2022) 2494–2502.
[11] J.D. Lopez, A. Dante, C.C. Carvalho, R.C.S.B. Allil, M.M. Werneck, Simulation and experimental study of FBG-based magnetic field sensors with Terfenol-D composites in different geometric shapes, Measurement (2021) 172.
[12] J. Xu, et al., Sensitivity Enhanced Magnetic Field Sensor Based on Hollow Core Fiber Fabry-Perot Interferometer and Vernier Effect, IEEE Photon. J. 14 (4) (2022) 1–5.
[13] C. Su, et al., A Highly Sensitive Sensor Based on Combination of Magnetostrictive Material and Vernier Effect for Magnetic Field Measurement, J. Lightw. Technol. 42 (1) (2022) 1–8.
[14] B. Sun, M. Bai, X. Ma, X. Wang, Z. Zhang, L. Zhang, Magnetic-Based Polydimethylsiloxane Cap for Simultaneous Measurement of Magnetic Field and Temperature, J. Lightw. Technol. 40 (8) (2022) 2625–2630.
[15] S.H. Mahmood, S.K. Al-Hayali, A. Al-Janabi, Wide-range pH sensor based on a cascaded MZI up-down tapered hetero-core structure, Applied Optics 63 (11) (2024) 2906–2915.
[16] F. Anelli, A. Annunziato, A.M. Loconsole, V.V. Francione, S. Cozic, S. Poulain, F. Prudenzano, Mid-infrared interferometry with non-adiabatic tapered ZBLAN optical fiber, Optics Express 32 (11) (2024) 18944–18957.
[17] W. Naku, O. Alsalman, C. Zhu, High-Sensitivity and Large-Range Displacement Sensor Based on a Balloon-Shaped Optical Fiber and Machine Learning Analysis, J. Lightw. Technol. (2024).
[18] N.C. Abd Rashid, N.A. Cholan, K.G. Tay, et al., Ammonia Detection in Water using Balloon-like Fiber Optic Sensor Coated with Oxazine and PDMS, Optik 171677 (2024).
[19] A. Majee, K. Dey, S. Roy, Role of lateral Core-Offset in the sensitivity enhancement of single Mode-No core-Single mode fiber cascaded structure, Optical Fiber Technology 85 (2024) 103812.
[20] R. Xu, Y. Xu, B. Luo, et al., Vector Magnetic Field Sensing Characteristics of the Magnetofluid-encapsulated Polarization-maintaining Fiber Single-end Offset Fusion Spliced Hollow-core Fiber Structure, IEEE Sensors Journal (2024).
[21] J. Xu, X. Tang, L. Xin, Z. Sun, T. Ning, High sensitivity magnetic field sensor based on hybrid fiber interferometer, Opt. Fiber Technol. 78 (2023) 103321.
[22] A. Rostami, et al., Advances in fibre Bragg grating technology for magnetic field sensing: A review, Measurement. 221 (2023) 113482.
[23] J. Philip, Magnetic nanofluids (Ferrofluids): Recent advances, applications, challenges, and future directions, Advances in Colloid and Interface Science 311 (2023) 102810.
[24] X. Ding, J. Yan, N. Chen, et al., Highly sensitive balloon-like fiber interferometer based on GO nanomaterial coated for humidity measurement, Optics & Laser Technology 158 (2023) 108798.
[25] X. Ding, T. Jin, R. Zhang, Balloon-like angle and micro-displacement sensor based on bent single-mode fiber, Optical Fiber Technology 68 (2022) 102787.
[26] X. Wang, Y. Zhao, R. Lv, et al., Magnetic field measurement method based on the magneto-volume effect of hollow core fiber filled with magnetic fluid, IEEE Transactions on Instrumentation and Measurement 70 (2021) 1–8.
[27] D. Šimić, A. Lang, M. Klüppel, Inductive and magnetorheological properties of soft and hard magnetic fillers in elastomers, Smart Materials and Structures 32 (12) (2023) 125016.
[28] T. Ioppolo, M.V. Ötügen, Magnetorheological polydimethylsiloxane micro-optical resonator, Optics Letters 35 (12) (2010) 2037–2039.
[29] Z. Li, J.M. Coote, S. Subburaman, et al., Low-field actuating magnetic elastomer membranes characterized using fibre-optic interferometry, Adv. Funct. Mater. 33 (50) (2023) 2301857.
[30] Z. Hao, et al., Dual-channel temperature-compensated vector magnetic field sensor based on lab-on-a-fiber-tip, Opt. Express 30 (2022) 25208–25218.
[31] Q. Zhang, H. Liu, R. Fu, et al., High sensitivity surface plasmon resonance magnetic field sensor based on Au/gold nanoparticles/magnetic fluid in the hollow core fiber, IEEE Sensors Journal (2023).
[32] Y. Zhu, C. Jiang, Y. Ma, et al., Ultrasensitive magnetic field sensor based on cladding-etched long-period grating, Optics Letters 48 (9) (2023) 2461–2464.
[33] H. Huang, C. Liao, M. Zou, et al., Four-dimensional printing of a fiber-tip multimaterial microcantilever as a magnetic field sensor, ACS Photonics 10 (6) (2023) 1916–1924.
[34] D. Zhang, H. Wei, H. Hu, et al., Highly sensitive magnetic field microsensor based on direct laser writing of fiber-tip optofluidic Fabry-Pérot cavity, APL Photonics 5 (7) (2020).
[35] Z. Guo, Y. Bai, W. Zhang, et al., Temperature compensated magnetic field sensor based on magnetic fluid infiltrated cascaded structure of micro-tapered long-period fiber grating and fiber Bragg grating, Sensors and Actuators a: Physical 358 (2023) 114425.
[36] X. Ding, S. Liu, M. Wang, et al., Highly sensitive magnetic field sensor using magnetic fluid filled dual-core photonic crystal fiber, Optics & Laser Technology 175 (2024) 110801.